An Embedded Bottom Boundary Layer Formulation for *Z*-Coordinate Ocean Models

Y. TONY SONG AND YI CHAO

Jet Propulsion Laboratory, California Institute of Technology, Pasadena, California

(Manuscript received 21 December 1998, in final form 24 June 1999)

ABSTRACT

An embedded bottom boundary layer (EBBL) scheme is developed to improve the bottom topographic representation in *z*-coordinate ocean general circulation models. The EBBL scheme is based on the combined techniques of an embedded topography-following slab, an explicit turbulent bottom boundary layer (BBL), and a generalized pressure gradient formulation. The coupling between the interior *z*-level model and the EBBL model is achieved by exchanging entrainment/detrainment and pressure gradients at the bottom layer surface, which allows temporal and spatial variations.

The EBBL is implemented into one of the most widely used *z*-coordinate models, the Modular Ocean Model (MOM). A test problem with a source of dense water on a slope is used. The new EBBL produces significantly more realistic plume spreading than the existing BBL scheme of Killworth and Edwards and is comparable to the results from a topography-following coordinate model (SCRUM), which is believed to be more suitable for such a problem. Calculation of the momentum budget demonstrates that the improved representation of the downslope pressure gradient formulation plays an important role in the simulations of dense slope flows.

Sensitivity experiments with different grid sizes, model parameters, and density contrast between the cold source water and the warm interior water are carried out to test the robustness of the EBBL scheme. In contrast to the BBL model of Killworth and Edwards, which tends to diffuse too much dense water along isobaths, the EBBL model allows dense water to sink across isobaths through a very thin bottom layer into the deep ocean. Even in the coarser-resolution case (¼° and 15 levels) the EBBL produces more realistic deep water than the existing BBL with higher resolution (⅛° and 30 levels), and at only one-eighth the computational cost. It is therefore concluded that the EBBL scheme presented here is cost effective and robust to model resolution and mixing parameters, and should be easily implemented in any nontopography-following coordinate ocean model.

1. Introduction

The global thermohaline circulation is driven by two sources of high-latitude dense water: the input of North Atlantic Deep Water in the northern North Atlantic and the outflow of Antarctic Bottom Water formed over the continental shelf of the Weddell Sea. These dense waters form giant ocean cataracts and carry about 5 Sv (1 Sv equals one million cubic meters of water per second) through a descent of 3 km or more (Whitehead 1989), and are believed to contribute significantly to the deep-water formation (Dickson and Brown 1994; Jungclaus and Backhaus 1994), and thereby to the global thermohaline circulation. There also has been considerable interest recently in flow through narrow gaps since many of these small channels control large-scale features in the ocean, such as the Strait of Gibraltar (Bryden and Kinder 1991; Price and Baringer 1994) and the Drake and Indonesian Passages (Broecker 1991).

Numerical models are widely used in oceanographic research and are now beginning to reach the point where realistic models on basin to global scale are possible (Haidvogel and Bryan 1992; McWilliams 1996; Semtner 1995). It is therefore important to have the dynamics of the numerical model represent the dynamics of the real ocean as accurately as possible. As topography is one of the most important factors in controlling oceanic circulation, its representation in the numerical model must be as accurate as possible. Despite the recent progress in improving the representation of bottom topography in the *z*-coordinate ocean models (Gerdes 1993; Beckmann and Döscher 1997; Gnanadesikan et al. 2000, manuscript submitted to *J. Phys. Oceanogr.*; Killworth and Edwards 1999), realistically representing the bottom topography remains one of the most challenging problems so far for ocean modelers (Roberts and Wood 1997; Winton et al. 1998).

The most widely used type of ocean model in large-scale modeling is the Bryan–Cox model (Bryan 1969; Cox 1984), in which the ocean bottom topography is approximated steplike by fixed vertical levels. In reality, much of the dense outflow takes place through narrow sills or channels, which are subgrid-scale in the model,

Corresponding author address: Y. Tony Song, Jet Propulsion Laboratory, California Institute of Technology, 4800 Oak Grove Drive, M/S 300-323, Pasadena, CA 91109.
E-mail: song@pacific.jpl.nasa.gov

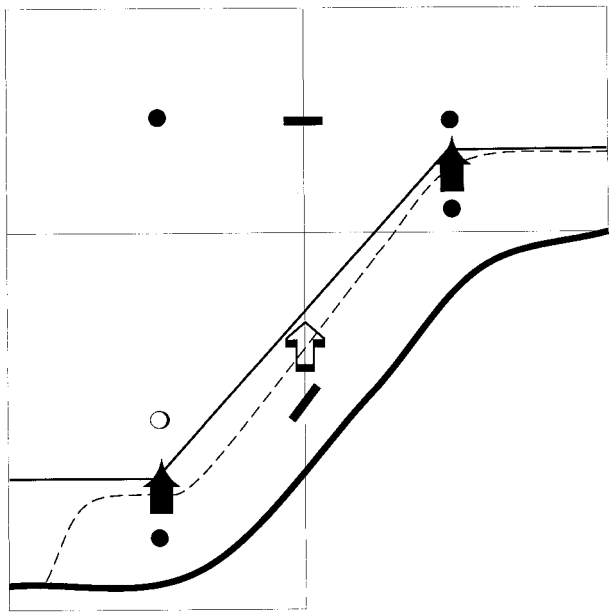

FIG. 1. Schematic of embedded bottom boundary layer (EBBL). Heavy bold line is the bottom topography, light bold line is embedded in the bottom grid cell (at the ¼ of the grid height below the lowest density point) and the dashed line is the surface of the BBL depth. Bars denote velocity locations, and dots and circles denote tracer locations, where only dots are used for calculating the bottom pressure gradient for the BBL. Bold arrow represents entrainment/detrainment and box arrow represents the coupling of the bottom pressure gradient.

and small changes in the model topography to reflect these sills or channels have considerable impact on the large-scale circulation. For example, the densest water formed in the North Atlantic basin originates in the Greenland–Iceland–Norway (GIN) basin and flows southward through narrow channels in the ridges between Greenland, Iceland, and Scotland. These waters form an important part of the total southward flow of deep dense water and play a significant part in controlling the thermohaline circulation in the North Atlantic and global ocean. Using a *z*-coordinate model, Roberts and Wood (1997) found that a small change in model topography could either cut off completely the mass flux between the Atlantic and the GIN basin or increase the mass flux too much across the ridges compared with observational estimates. A similar argument also applies to the Mediterranean outflow and its interaction with the North Atlantic circulation.

Another related problem is the downslope transport of dense water, which is critical for producing adequate deep-water mass in ocean circulation models. Beckmann and Döscher (1997) found that the *z*-coordinate model with the steplike representation of the bottom boundary has a conceptual problem to simulate processes that depend on sloping topography, especially for coarse-resolution models. Downslope transport is treated as a series of advective and convective events, and there is a significant dilution of any water mass crossing isobaths. Hughes (1995) also identified an anomaly in the way the Cox (1984) code handles steep topography in which steps of more than one vertical grid point are present, resulting in a decoupling of the density field, which drives the barotropic flow from the component that is advected by the barotropic flow. In the steep slope regions where density is being advected, there will be a change in the Joint Effect of Baroclinicity and Relief (JEBAR) term, and therefore a change in the flow field

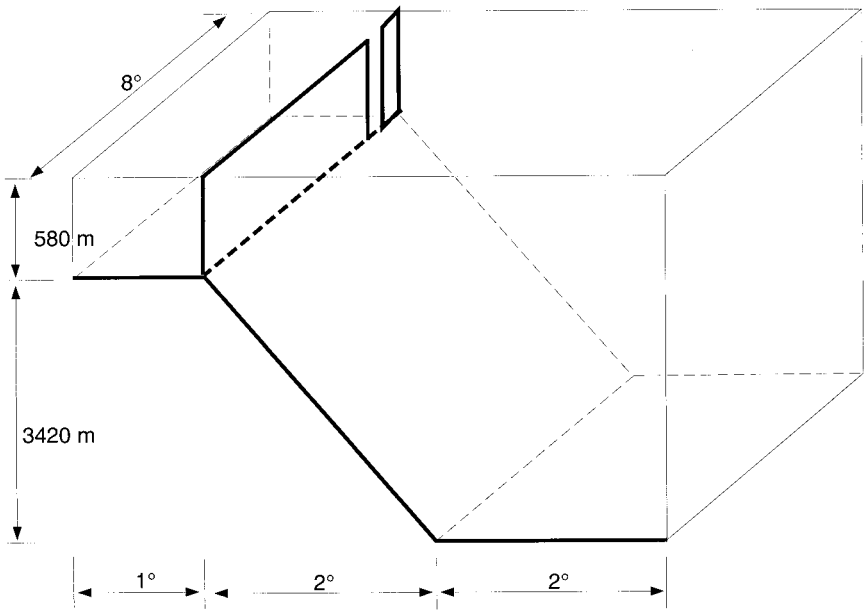

FIG. 2. Perspective view of the model domain for the test problem.

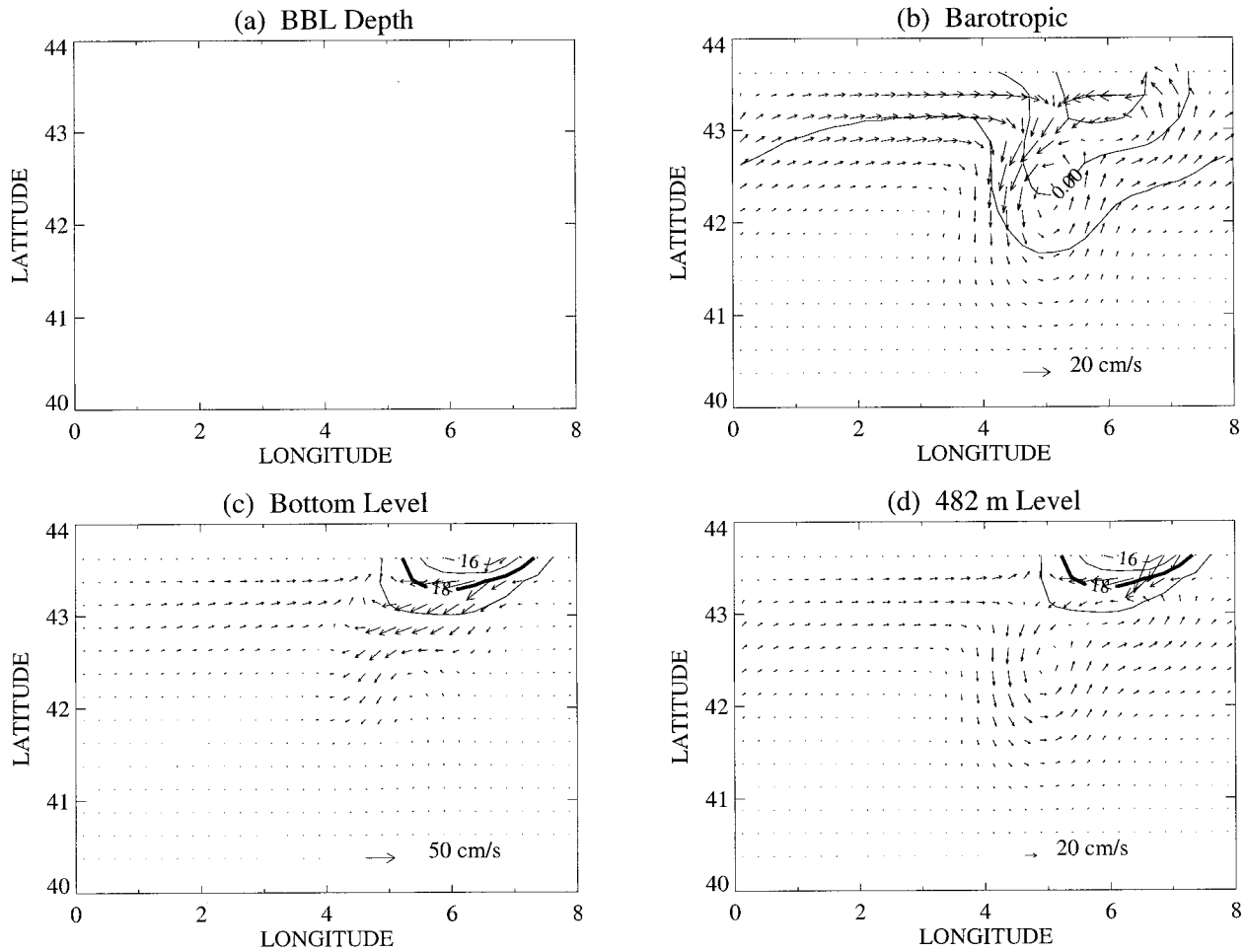

FIG. 3. Results after 30 days of integration with the free-surface MOM model (without BBL, Killworth et al. 1991) run. Shown are (a) depth of bottom boundary layer (zero in this case as no BBL is coupled), (b) free surface elevation and barotropic velocity, (c) bottom-most level temperature and velocity (mean value of the shaved bottom cell and the BBL cell), and (d) temperature and velocity at 482-m depth.

and the advection of density. This feedback loop can be important in transferring momentum input from surface wind forcing to the bottom of the ocean, so interference with this feedback loop can produce globally important consequences. Clearly the model representation of steep topography needs be improved.

In addition to the steep topographic effects, proper treatments of large-scale and gently varying topography are equally important for modeling the ocean general circulation because of its role in generating form stress (Haidvogel and Beckmann 1998) and bottom friction sink in the momentum budget (Treguier and McWilliams 1990). The inaccurate representation of kinematic boundary conditions in *z*-coordinate models has been examined by Gerdes (1993), who found that the model topography very often contains distributions of flat bottom areas by regions with steep slopes, which result from the misrepresentation of a gradually sloping bottom by a discrete set of possible depths. Associated with the localized large depth gradients are localized large vertical velocities, which are effectively seen by the model as a δ-function forcing at the lower boundary. The discretization of the kinematic boundary condition in *z*-coordinate models involves a truncation error, which causes potentially large errors in the vertical velocity field. As large-scale topography provides the largest form stress, some gentle and large-scale slopes of the ocean bottom are neglected by the *z*-coordinate models, and the main eastward momentum sink in the bottom layer was no longer the bottom friction drag but rather the topographic form stress resulting from different pressure forces on each side of the topography (Treguier and McWilliams 1990).

In short, the crude steplike approximation of topography can cause three major problems.

1) Downslope transport of dense water is treated as a series of advective and convective events, and there is a significant dilution of water mass crossing isobaths, with subsequent alteration of deep-water formation (Beckmann and Döscher 1997).

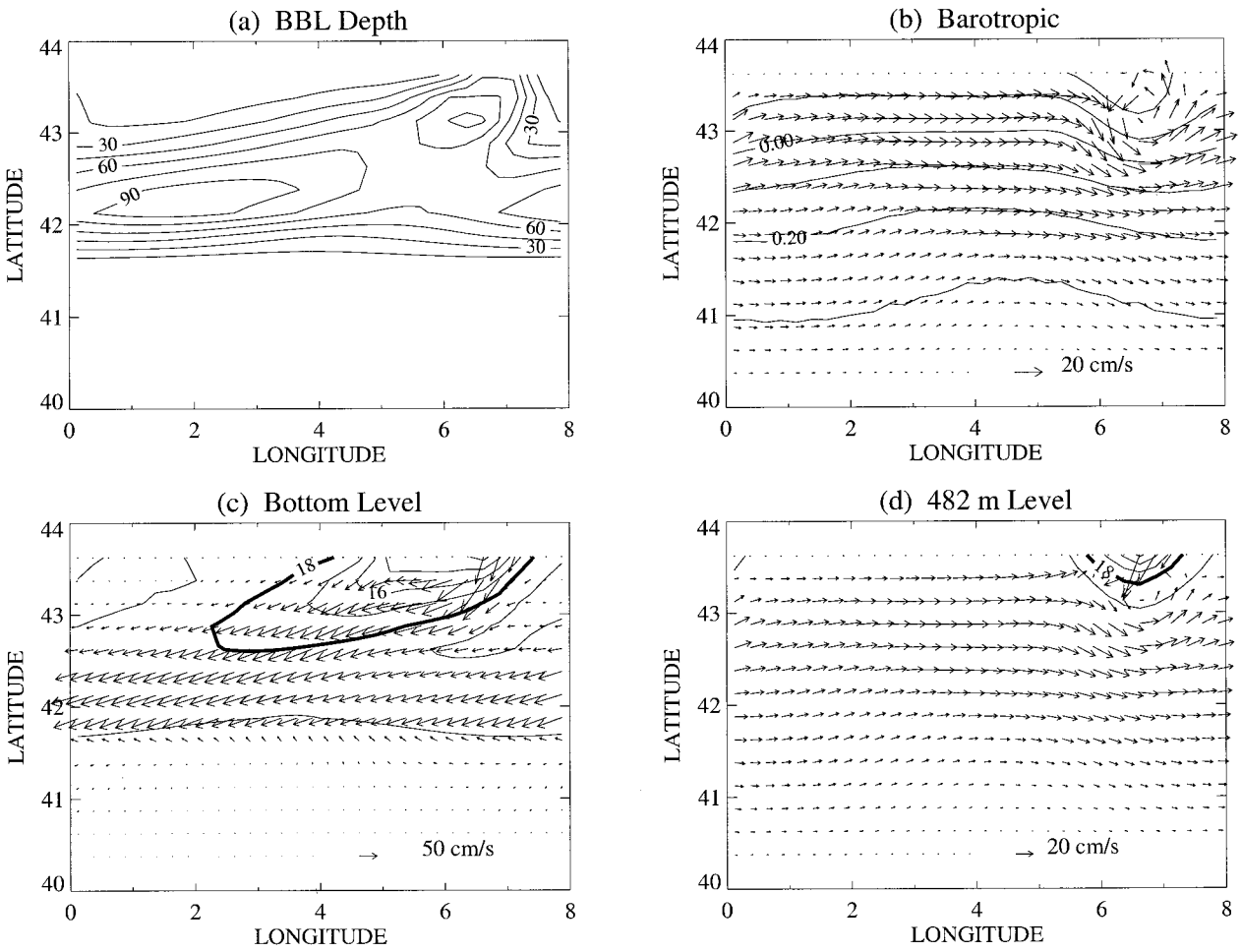

FIG. 4. Results after 30 days of integration with KE99 BBL. Shown are (a) depth of bottom boundary layer, (b) free surface elevation and barotropic velocity, (c) bottom-most level temperature and velocity (mean value of the shaved bottom cell and the BBL cell), and (d) temperature and velocity at 482-m depth.

2) Because observed bathymetry is projected onto a series of fixed model levels, misrepresenting model topography for some critical sills and channels can have large impact on the outflow as the transport is highly dependent on the position and shape of the topography (Roberts and Wood 1997).
3) The discretization of the kinematic boundary condition in *z* models introduces truncation error, which causes potentially large errors in the vertical velocity field and affects the advection of density (Gerdes 1993).

A number of studies have been undertaken to improve the topographic representation problem in *z*-coordinate models. Adcroft et al. (1997) proposed a shaved cell technique for the nonhydrostatic model of Marshall et al. (1997). Beckmann and Döscher (1997) incorporated a coupled terrain-following bottom boundary layer model for the tracer equations to improve the downslope spreading of dense waters in the Bryan–Cox model. Gnanadesikan et al. (2000, manuscript submitted to *J. Phys. Oceanogr.*) extended their approach by including the momentum equations in the boundary layer. Further, Killworth and Edwards (1999) incorporated a turbulent bottom boundary layer (BBL) model to the free-surface version of the Bryan–Cox model, which allows entrainment and detrainment processes at the interface of the spatial- and time-varying bottom layer. This series of efforts has shown significant improvement of topographic representation of *z*-coordinate models in their idealized tests, though their effectiveness in realistic applications remains to be demonstrated.

In this paper, we propose an embedded bottom boundary layer (EBBL) scheme for *z*-coordinate ocean models, based on the combined techniques of an embedded topography-following slab (Beckmann and Döscher 1997), an explicit turbulent bottom boundary layer (Killworth and Edwards 1999) within the slab, and a generalized pressure gradient formulation (Song 1998). The paper is organized as follows. In section 2 we describe our EBBL scheme and the numerical implemen-

tation into a free surface Bryan–Cox model (Killworth et al. 1991). Section 3 presents the test problem results and comparisons with results from the existing BBL of Killworth and Edwards (1999, hereafter referred to as KE99) and from SCRUM (Song and Haidvogel 1994). The sensitivity and momentum budget analysis are discussed in section 4, and section 5 concludes this paper.

2. Model and EBBL Description

a. Basic model equations

Before working through the methodology of our EBBL scheme, we first introduce the hydrostatic, Boussinesq primitive equations formulated on the z-coordinate system. Following Bryan (1969) and Cox (1984), the momentum equations are

$$\frac{\partial u}{\partial t} + \mathbf{v}\cdot\nabla u - fv = -\frac{1}{\rho_0}\frac{\partial p}{\partial x} + \frac{\partial}{\partial z}\left(K_M\frac{\partial u}{\partial z}\right) + \mathcal{D}_u + \mathcal{F}_u \quad \text{and} \tag{2.1}$$

$$\frac{\partial v}{\partial t} + \mathbf{v}\cdot\nabla v + fu = -\frac{1}{\rho_0}\frac{\partial p}{\partial y} + \frac{\partial}{\partial z}\left(K_M\frac{\partial v}{\partial z}\right) + \mathcal{D}_v + \mathcal{F}_v, \tag{2.2}$$

the temperature and salinity equations are

$$\frac{\partial T}{\partial t} + \mathbf{v}\cdot\nabla T = \frac{\partial}{\partial z}\left(K_H\frac{\partial T}{\partial z}\right) + \mathcal{D}_T + \mathcal{F}_T \quad \text{and} \tag{2.3}$$

$$\frac{\partial S}{\partial t} + \mathbf{v}\cdot\nabla S = \frac{\partial}{\partial z}\left(K_H\frac{\partial S}{\partial z}\right) + \mathcal{D}_S + \mathcal{F}_S, \tag{2.4}$$

the approximated hydrostatic pressure is

$$\frac{\partial p}{\partial z} = -g\rho(T, S, z), \tag{2.5}$$

and the continuity equation is

$$\frac{\partial u}{\partial x} + \frac{\partial v}{\partial y} + \frac{\partial w}{\partial z} = 0. \tag{2.6}$$

We have used x, y, z as Cartesian coordinates with the z axis pointing vertically upward and the x–y plane occupying the undisturbed water surface. Equations (2.1)–(2.6) are, respectively, conservation of east and north momentum, heat and salt, the hydrostatic relation, and zero flow divergence. The notations used in these equations are as follows:

u, v, w	the x, y, z components of vector velocity $\mathbf{v}$;
$T(x, y, z, t)$	temperature;
$S(x, y, z, t)$	salinity;
$\rho_0 + \rho(x, y, z, t)$	density;
p	pressure;
f	Coriolis parameter $2\Omega \sin\theta$;
g	acceleration due to gravity;
$K_M(x, y, z, t)$	vertical eddy viscosity;
$K_H(x, y, z, t)$	vertical eddy diffusivity;
$\mathcal{D}_u$, $\mathcal{D}_v$, $\mathcal{D}_T$, $\mathcal{D}_S$	horizontal viscous and diffusive terms; and
$\mathcal{F}_u$, $\mathcal{F}_v$, $\mathcal{F}_T$, $\mathcal{F}_S$	forcing terms.

Although the equations are solved in spherical polar coordinates as in Bryan and Cox's original formulation, here we use Cartesian coordinates for simplicity. Following KE99, these equations hold in the interior of the fluid, between the free surface $z = \eta(x, y, t)$ (the code is based on a free surface version, though a rigid lid can equally well be used) and a height $h(x, y, t)$ above the bottom $z = -D(x, y)$, where $h(x, y, t)$ is the moving thickness of the bottom boundary layer, and will be introduced in the following section.

b. Embedded Bottom Boundary Layer (EBBL)

A schematic of the EBBL scheme is shown in Fig. 1. The topography-following slab is similar to that used by Beckmann and Döscher (1997). Here the bottom level of the slab can follow the continuous real topography (before modified by vertical levels) and the top level of the slab is set ¼ of the bottom grid below the lowest density point (see Fig. 1). The reason for allowing the bottom layer to follow the real topography is to avoid sensitivity to vertical level resolution, as reported by Roberts and Wood (1997). Within the slab, a turbulent bottom boundary layer, shown as a dashed line, is attached to a computational level, where the dots denote tracer locations and bars denote velocity locations. It should be noted that multilevel layers can be applied within the slab if necessary, though here we only use one layer for simplicity.

Within the bottom slab, momentum and tracers are required to satisfy the following equations:

$$\frac{\partial h}{\partial t} + \nabla\cdot(h\mathbf{u}_B) = 0, \tag{2.7}$$

$$\frac{\partial hu_B}{\partial t} + \nabla\cdot(h\mathbf{u}_B u_B) - fhv_B = -\frac{h}{\rho_0}\frac{\partial p_B}{\partial x} + \nabla\cdot(A_H h\nabla u_B) + w^* u_I - C_D|\mathbf{u}_B|u_B, \tag{2.8}$$

$$\frac{\partial hv_B}{\partial t} + \nabla\cdot(h\mathbf{u}_B v_B) + fhu_B = -\frac{h}{\rho_0}\frac{\partial p_B}{\partial y} + \nabla\cdot(A_H h\nabla v_B) + w^* v_I - C_D|\mathbf{u}_B|v_B, \tag{2.9}$$

$$\frac{\partial hT_B}{\partial t} + \nabla\cdot(h\mathbf{u}_B T_B) = \nabla\cdot(A_H h\nabla T_B) + w^* T_I, \quad \text{and} \tag{2.10}$$

$$\frac{\partial hS_B}{\partial t} + \nabla\cdot(h\mathbf{u}_B S_B) = \nabla\cdot(A_H h\nabla S_B) + w^* S_I, \tag{2.11}$$

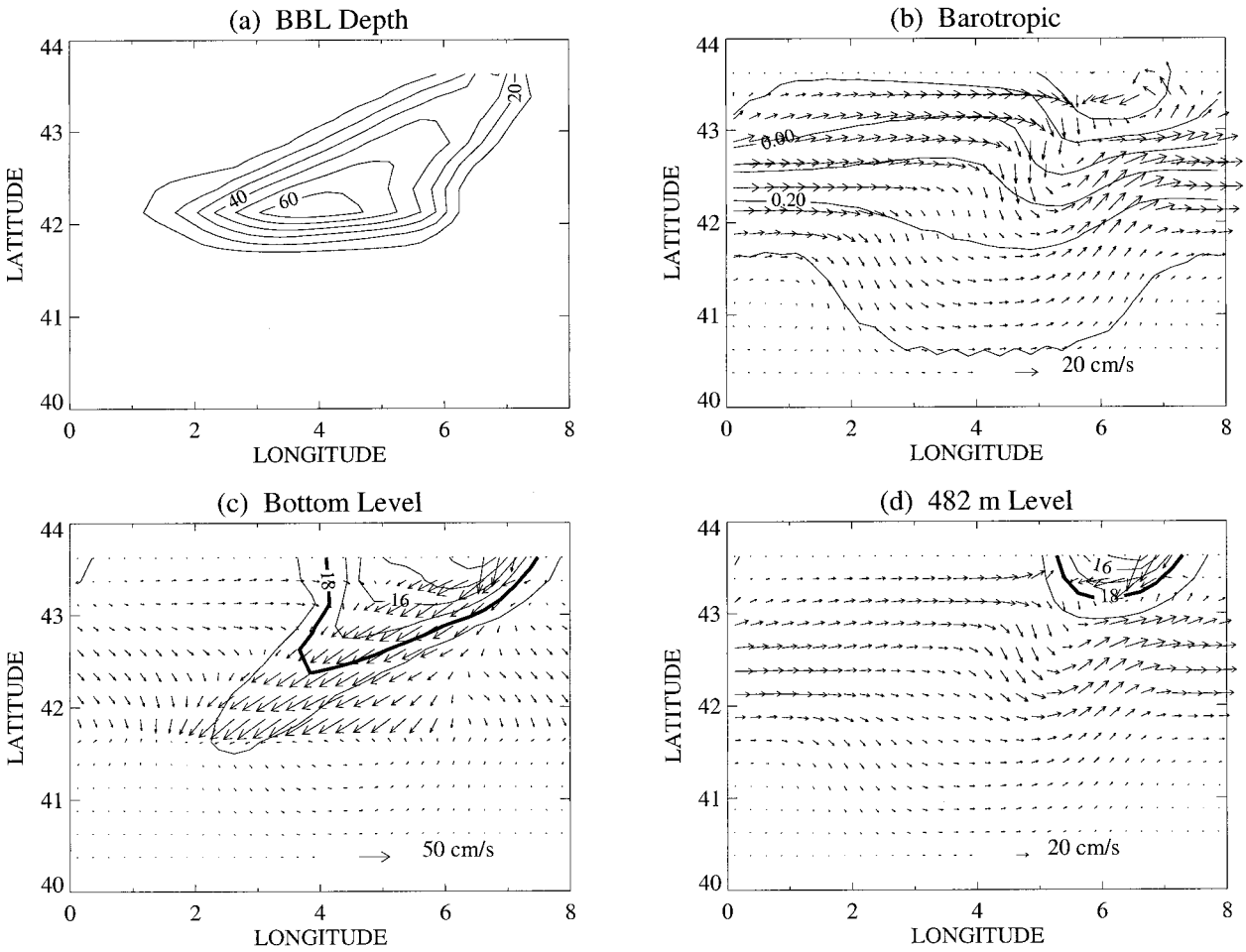

FIG. 5. As in Fig. 4 but with the new EBBL. The maximum depth of the BBL in (a) is 65 m and the contour interval is 10 m. (b) A stronger cyclonic eddy induced by the plume is shown in the surface elevation and barotropic velocity field. The thick line in (c) and (d) is the 18°C isotherm.

where suffixes I and B denote interior and boundary values, respectively; C_D is the bottom drag coefficient; and w^* denotes the entrainment/detrainment velocity at the surface of the bottom boundary layer. It should be pointed out that the primitive equations (2.1)–(2.6) hold only in the interior of the fluid, between the free surface and the moving bottom boundary layer height $h(x, y, t)$ above the ocean bottom $z = -D(x, y)$. Rather than the normal bottom boundary conditions, vertical turbulent fluxes vanish at $z = -D(x, y)$; they are replaced by the effects of entrainment/detrainment at $z = -D(x, y) + h(x, y, t)$. The bottom layer Eqs. (2.7)–(2.11) are formulated in the standard x, y, and z coordinates, which are different with the topography-following formulation of Trowbridge and Lentz (1991).

The BBL height $h(x, y, t)$ is calculated in two steps. First, it is calculated by Eqs. (2.7)–(2.11) to conserve momentum and tracers. The momentum and tracer equations are solved using the same numerical method as in solving the interior equations, while the bottom boundary layer depth equation is solved by an explicit leapfrog time stepping with a weak Asselin filter method. The boundary layer depth has thus changed because of large-scale divergence or convergence of the flux in the layer.

To include the turbulent effects, the depth of the BBL is evaluated diagnostically at every time step by the modified Zilitinkevich and Mironov (1996) formula

$$\left(\frac{h}{C_n u_*/f}\right)^2 + \frac{h}{C_i u_*/N} = 1, \qquad (2.12)$$

where the bottom friction velocity is $u_* = \sqrt{C_D}|\mathbf{u}_B|$, N is the background buoyancy frequency, $C_n = 0.5$, and $C_i = 20$.

The change between the formula value and that obtained from the large-scale dynamics is considered to represent the effects of entrainment if the layer has deepened, or detrainment if the layer has become thinner. Tracers and momentum are simply removed from the interior and mixed into the boundary layer if the layer is entraining. A more detailed description of the en-

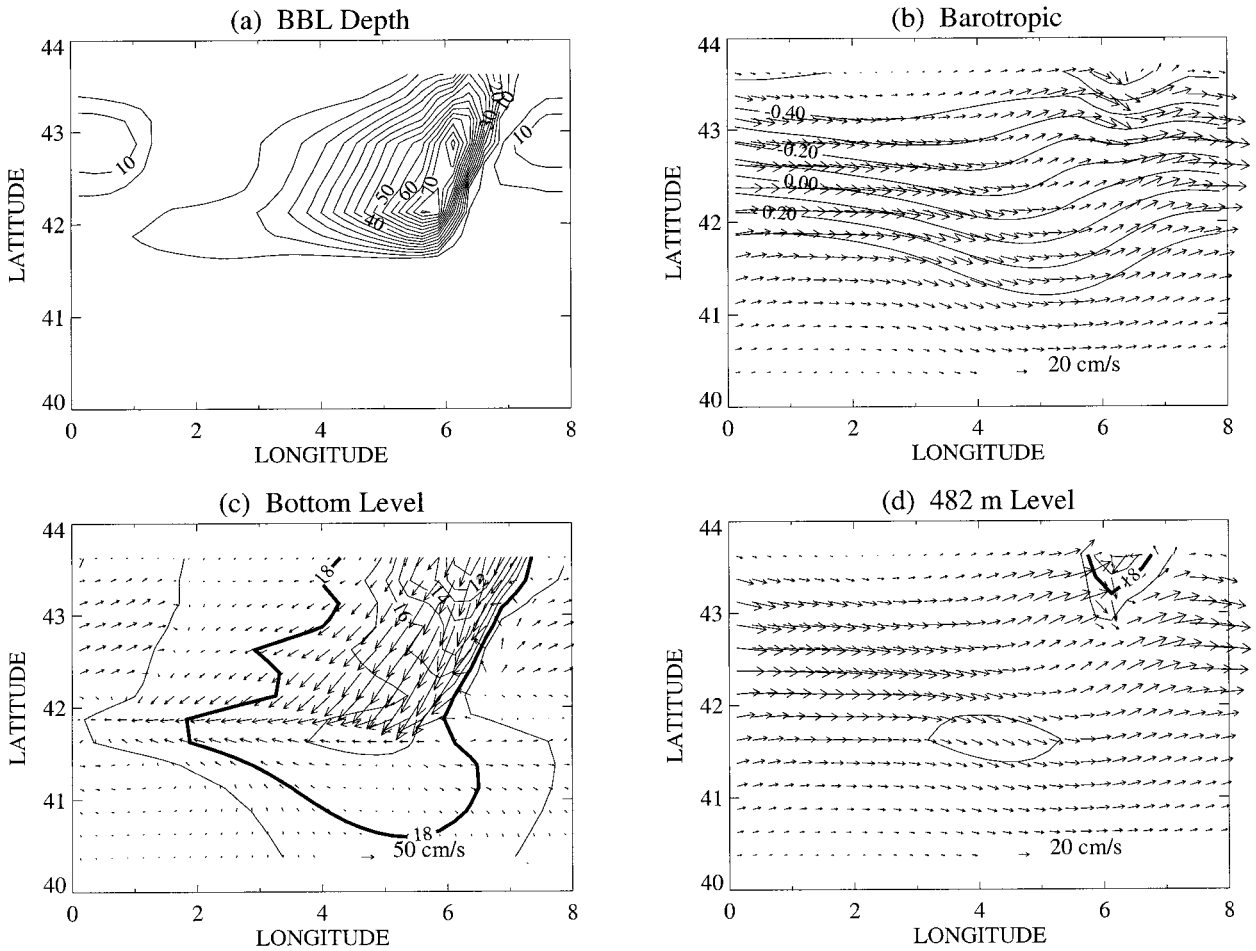

FIG. 6. As in Fig. 4 but results from SCRUM using the Mellor–Yamada Level-II turbulence closure scheme for the BBL. The depth of the BBL is the height at which the turbulent kinetic energy goes to zero.

trainment and detrainment processes is given in Killworth and Edwards (1999).

It should be noted that Eq. (2.12) can be solved as

$$h = \frac{C_h u_*}{f}\{-C_k N/f + \sqrt{(C_k N/f)^2 + 1}\}, \quad (2.13)$$

where $C_k = C_n/(2C_i)$. By using a more sophisticated Mellor–Yamada Level-II turbulence closure scheme, Weatherly and Martin (1978) obtained that the depth of the BBL can be identified with the height at which the turbulence mixing goes to zero and is approximated by $h = 1.3u_*/[f(1 + N^2/f^2)^{1/4}]$. These two formulas agree quantitatively over the range $10 \le N/f \le 100$ (a reasonable range for the ocean). They also agree qualitatively over the range $0 \le N/f \le 100$ in the sense that the BBL depth decreases as N/f increases.

c. Pressure gradient formulation

Most of the deep water in the World Ocean enters the abyss by descending along continental slopes in thin (approximately 100 m) density-driven plumes. To resolve such a thin slope bottom boundary layer, ocean models, especially their pressure gradient terms, should be formulated in a careful way. However, it is found that the difficulty of maintaining the density signal as the plume descends the slope is the main impediment to accurate simulation in ocean models (Haney 1991; Winton et al. 1998).

For example, in σ-coordinate models, the pressure gradient force is traditionally determined by the sum of two terms (Arakawa and Suarez 1983), that is,

$$\left.\frac{\partial p}{\partial x}\right)_z = \frac{\partial p}{\partial x} - \frac{\sigma}{h}\frac{\partial p}{\partial \sigma}\frac{\partial h}{\partial x}, \quad (2.14)$$

where $\sigma \equiv z/h$. The first term on the right involves the variation of pressure along a constant σ surface and the second involves the usual vertical variation of pressure. Near steep topography these terms are large, comparable in magnitude, and typically opposite in sign. In such cases, a small error in computing either term can result in a large error in the total horizontal pressure gradient force. While in z-coordinate models, although there is no pressure gradient error, the slope bottom boundary

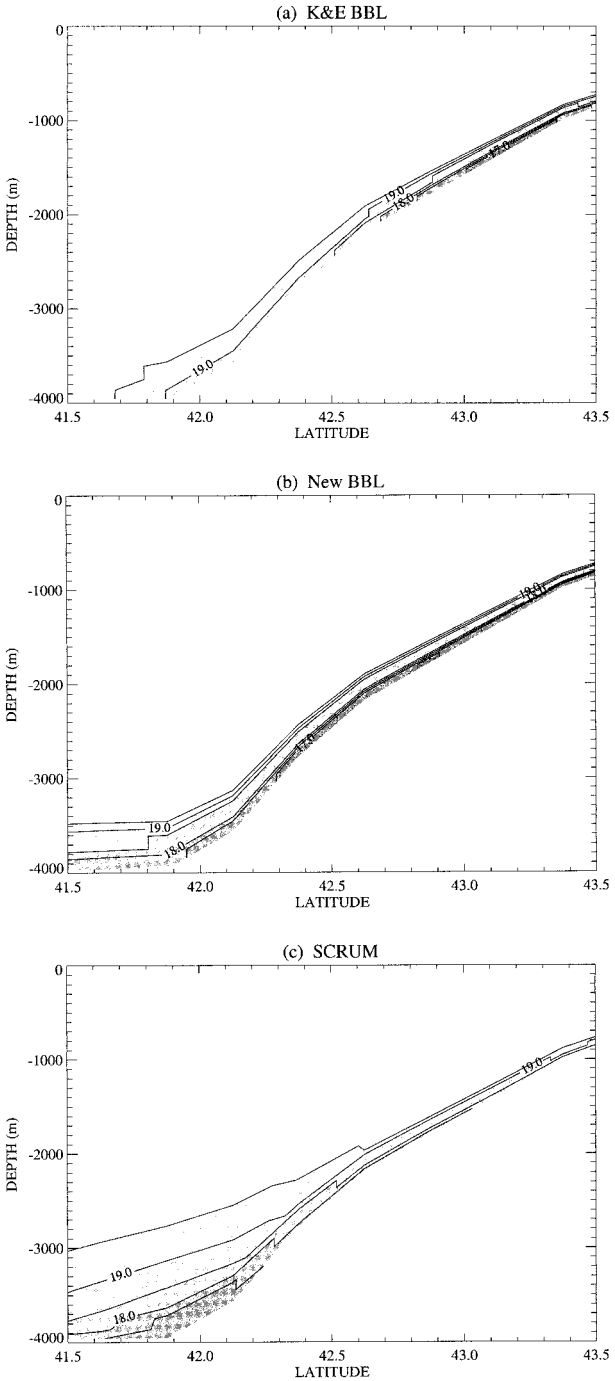

FIG. 7. Cross-slope section for temperature anomaly after 30 days of integration. Shown are (a) from KE99 BBL, (b) from the new EBBL, and (c) from SCRUM. Contour interval is 0.5°C.

is not resolved at all as it is approximated by a series of steps.

As we noted, the pressure gradient terms in the interior Eqs. (2.1)–(2.2) are formulated in z-coordinate levels, while the corresponding terms in the BBL level follow the bottom slab. It is our intention in this section to develop a pressure gradient scheme to couple these two systems consistently and accurately.

Recently, Song (1998) proposed a Jacobian formulation of pressure gradients for a general vertical coordinate system. His formulation can be written as

$$\left.\frac{\partial p}{\partial x}\right)_z = \frac{\partial p_s}{\partial x} + g\int_s^0 \left\{\frac{\partial z}{\partial s'}\frac{\partial \rho}{\partial x} - \frac{\partial z}{\partial x}\frac{\partial \rho}{\partial s'}\right\} ds', \quad (2.15)$$

where s represents any vertical coordinate and the first term in the right-hand side of the equation represents the surface pressure gradient. The ‘‘$)_z$’’ symbol emphasizes that the derivative is carried out with z held constant. The expression in the brackets is the Jacobian

$$J(z, \rho) = \frac{\partial z}{\partial s}\frac{\partial \rho}{\partial x} - \frac{\partial z}{\partial x}\frac{\partial \rho}{\partial x}. \quad (2.16)$$

It should be noted that the formulation in terms of a Jacobian is significant since it is clearly independent of the particular form of the vertical coordinate. For example, in the z coordinate system, $s = z$, then $J(z, \rho) = \partial\rho/\partial x)_s = \partial\rho/\partial x)_z$ gives the original pressure gradients; in the σ-coordinate system, $s = \sigma = (z - \zeta)/H$, then $J(z, b) = H(\partial\rho/\partial x) - (\partial\rho/\partial\sigma)(\partial\sigma H/\partial x)$, where $H = h + \zeta$, recovers the topography-following scheme. For this reason, this formulation can be used to couple the two coordinate systems in a consistent way. Therefore, we can derive the pressure gradient formulation in the bottom boundary layer as the following:

$$\left.\frac{\partial p_B}{\partial x}\right)_z = \frac{\partial p_I}{\partial x} + g\int_{s_B}^{s_I} \left\{\frac{\partial z}{\partial s'}\frac{\partial \rho}{\partial x} - \frac{\partial z}{\partial x}\frac{\partial \rho}{\partial s'}\right\} ds', \quad (2.17)$$

where the surface pressure is replaced by the pressure at the interface and s' varies between $s_I = -D(x, y) + h(x, y, t)$ and $s_B = -D(x, y)$, as shown in Fig. 1.

Note that the z-coordinate level is naturally coupled with the topography-following coordinate system in the formulation. The first term in the right-hand side of the formulation is the original pressure gradient as in the Bryan–Cox code but modified for coupling to the EBBL as

$$\frac{\partial p_I}{\partial x} = \frac{\partial p_b}{\partial x} - gh\frac{\partial \rho}{\partial x}, \quad (2.18)$$

where P_b is the pressure in the bottom cell of the original Bryan–Cox code. The second term in the above two equations becomes significant only when the bottom boundary layer exists and coupling is necessary.

This formulation can be applied in the case of multiple bottom topography-following layers. For the case where only one level is used in the bottom boundary layer, the pressure difference across the grid cell (see Fig. 1) for the bottom layer can be simplified as

$$PX_B = PX_I + g(\delta_s\overline{z}^x\delta_x\overline{\rho}^s - \delta_x\overline{z}^s\delta_s\overline{\rho}^x), \quad (2.19)$$

where PX_I is the discrete form of interior pressure dif-

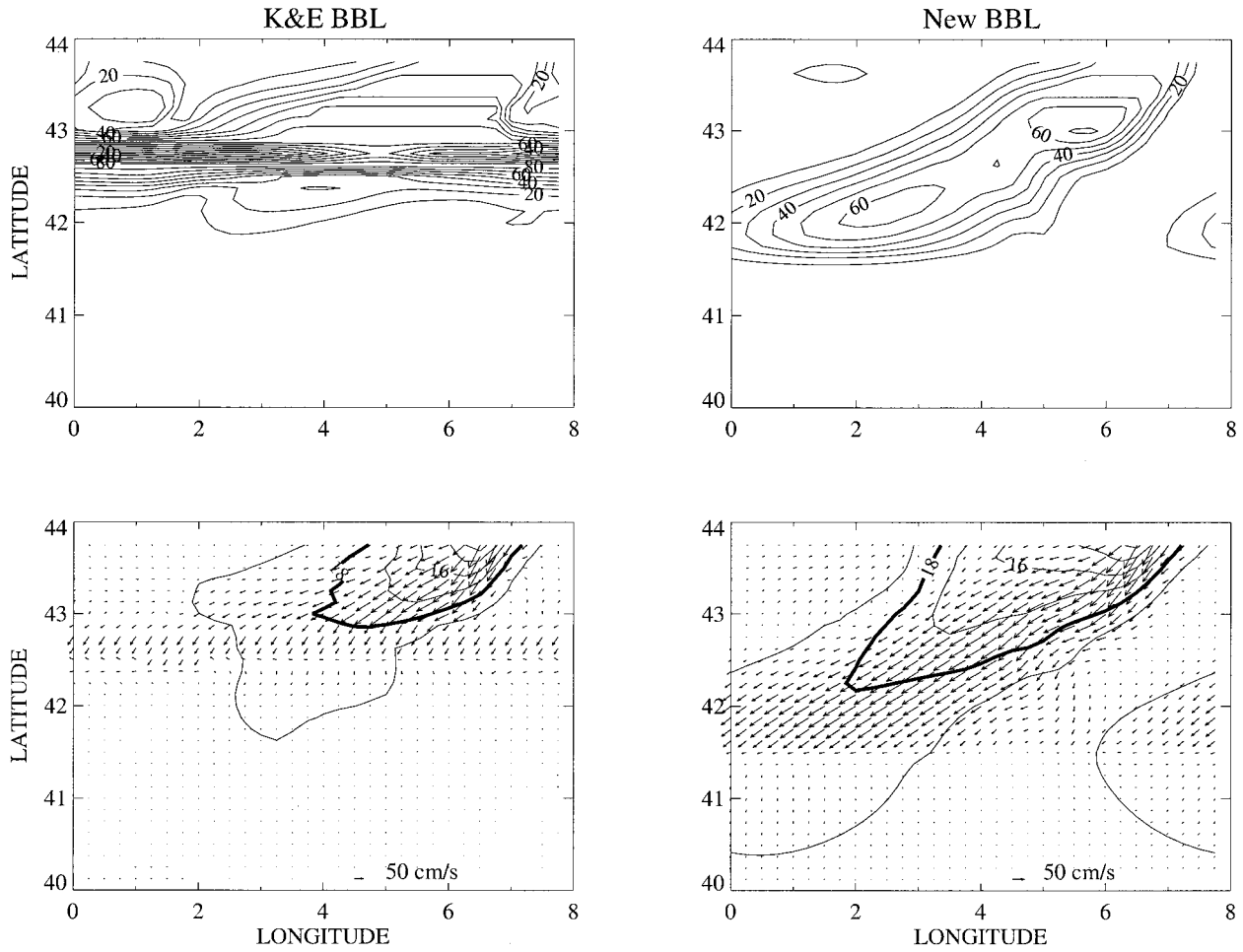

FIG. 8. Model results after 30 days with increased resolution by a factor of 2 in each spatial direction and time. Shown are depth of bottom boundary layer (upper panels), bottom boundary layer temperature and velocity (lower panels), left panels from KE99 BBL, and right panels from the new EBBL.

ference (2.18), the second term is the discrete Jacobian. The following notations are used:

$$\delta_x b = b_{i+1} - b_i, \qquad \delta_s b = b_I - b_B,$$

$$\overline{b}^x = \frac{1}{2}(b_i + b_{i+1}), \quad \text{and} \quad \overline{b}^s = \frac{1}{2}(b_I + b_B), \qquad (2.20)$$

where indices i represent locations of density ρ and I represents the interface box, which in this case is the bottom grid cell. It can be seen that Eq. (2.19) is simple and cost effective.

Song (1998) has shown that the Jacobian formulation (2.15) is significantly more accurate than the conventional formulation (2.14). One of the main reasons is that the numerical errors tend to cancel each other for those two symmetric terms in the Jacobian form. For example, errors associated with linear isopycnal perturbations (e.g., $\rho = cz$) are zero in form (2.15), but nonzero in form (2.14), as shown by Haney (1991) in the case of nonuniformed vertical grid size (which is true in our case).

In addition, ocean models are required to conserve physical properties of the continuous equations, such as momentum and total energy. Song and Wright (1998) have shown that the Jacobian pressure gradient formulation of (2.17) conserves momentum, total energy, and the bottom pressure torque in both analytical and discrete forms with any vertical coordinate system. The conservation of important physical properties in the continuous equations (2.7)–(2.11) has been addressed in Killworth and Edwards (1999). A combination of Eqs. (2.7)–(2.11) and (2.17) also conserve the physical properties, but the detailed derivations are not included in this paper.

3. Model results and validations

In this section, we use the same test problem as used by Killworth and Edwards (1999) to examine the model performance. The model domain consists of two connected basins, one cold basin with 1° width in the north and another warm basin with 4° width in the south,

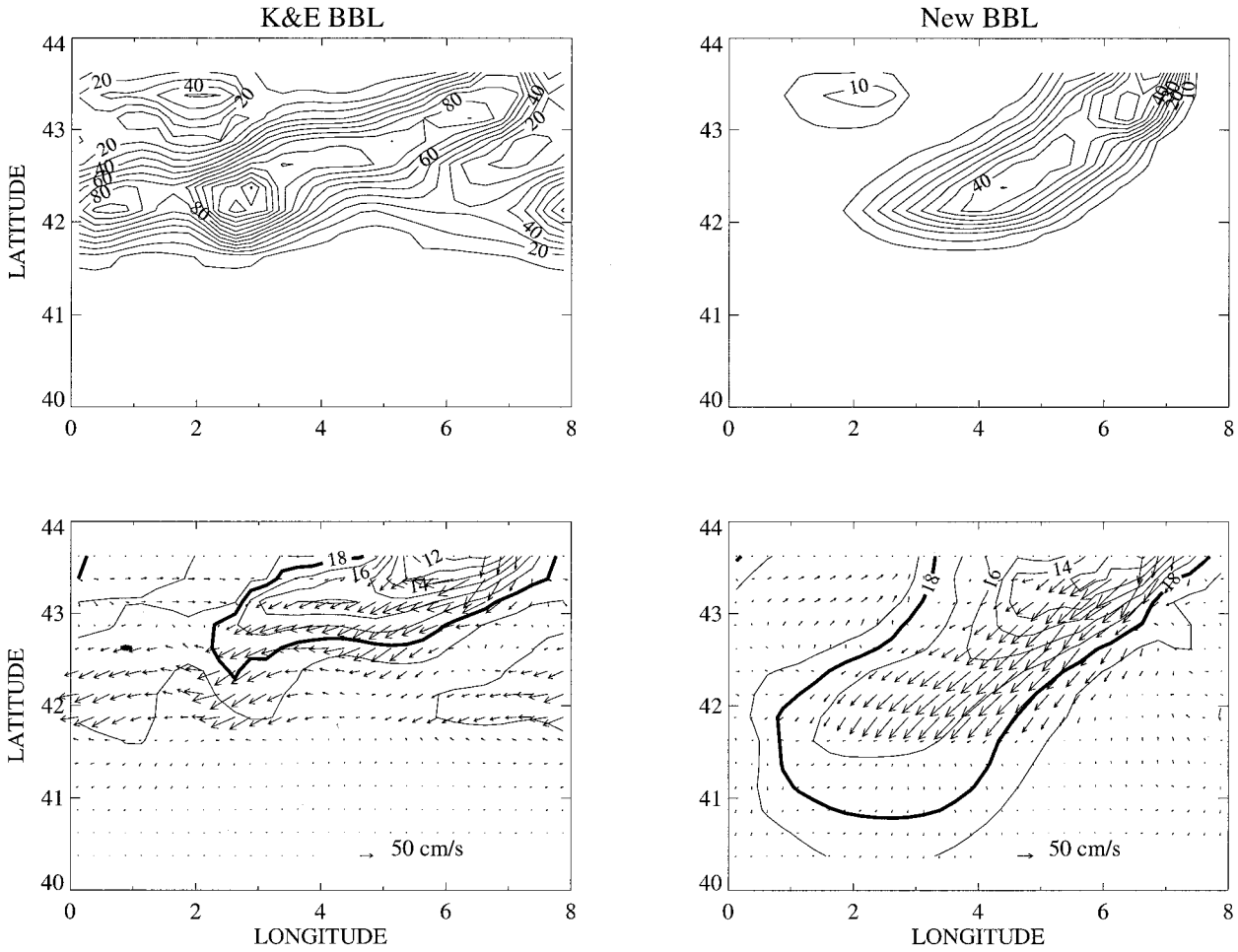

FIG. 9. Model results after 30 days with reduced viscosity and diffusivity by a half. Shown are depth of bottom boundary layer (upper panels), bottom boundary layer temperature and velocity (lower panels), left panels from KE99 BBL, and right panels from the new EBBL.

centered at 42°N, as shown in Fig. 2. The two basins are 8° long and are connected by a strait of 1° width. The cold basin is shallower with a constant depth of 580 m, which represents denser coastal or shelf water as the salinity is set to be constant for the two basins. The warm basin has a topography varying in the meridional direction only, from the 580-m depth in the north to 4-km depth at 42°N, representing the slope between the basins and the deep ocean. The maximum slope is about 4%.

The lateral boundary conditions for the model domain are zero flux and no slip wall at the northern and southern boundaries, and periodic at the eastern and western boundaries. The nice feature of this simple test problem is that it allows the model to adjust itself by transporting cool water at lower layers to the deep ocean in exchange for warmer water from upper layer, rather than by specified inflow, which forces the system. The dynamical processes associated with coastal density fronts and dense water plumes have been investigated in recent years with a variety of numerical ocean models (Jungclaus and Backhaus 1994; Whelless and Klinck 1995; Middleton and Ramsden 1996). The dense coastal water at the bottom is expected to flow downslope, being self-advected to the right and forming a plume. Details of the plume shape and translational speed of the plume head will depend on the topographic slope, rate of rotation, initial anomaly thickness and density contrast, entrainment rate, values of bottom friction, lateral, and vertical viscosity and diffusivity. It is not our intention to study in detail the plume dynamics, but rather to use the known process to test our proposed EBBL scheme.

The model has 14 levels in the vertical, including the bottom layer, with vertical spacing increasing from 30 m at the uppermost level to 740 m at the deepest. Our standard experiment has a temperature contract of 10°C, with an initial temperature of 10°C in the cold basin and 20°C in the warm basin. The salinity is constant with a value of 32 ppt. Surface fluxes of momentum are set to zero, and the surface temperature is relaxed towards its initial value using a relaxation timescale of 50 days. Constant horizontal and vertical viscosities of

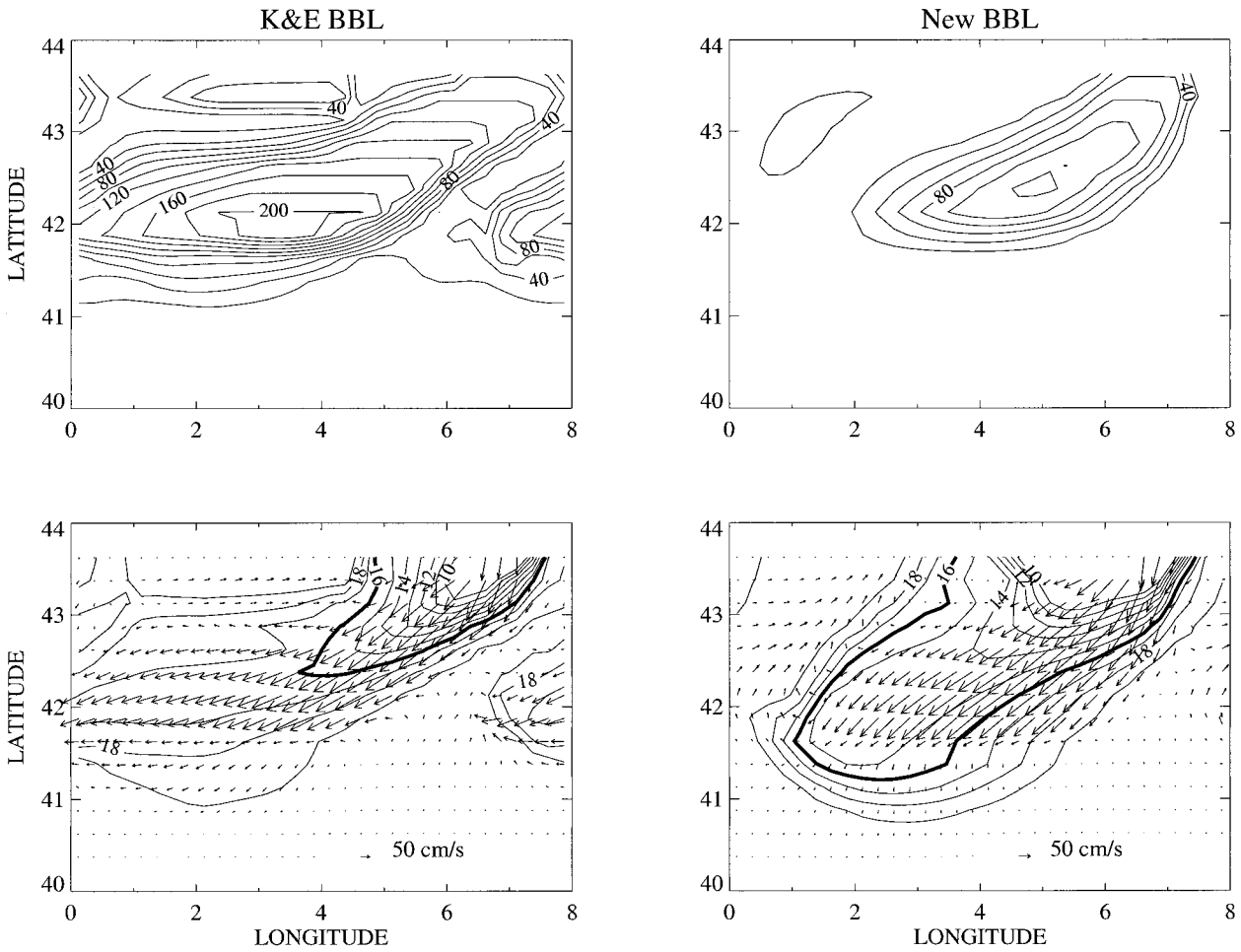

FIG. 10. Model results after 10 days of integration with increased density contrast (0°–20°C). Shown are depth of bottom boundary layer (upper panels), bottom boundary layer temperature and velocity (lower panels), left panels from KE99 BBL, and right panels from the new EBBL.

10^4 and 2×10^{-3} m^2 s^{-1} are used. The horizontal and vertical diffusivities are 2×10^3 and 10^3 m^2 s^{-1}. A quadratic bottom friction coefficient 3×10^{-3} is used.

The model is run prognostically for 30 days, with the results shown in Figs. 3–5, respectively, for the following cases: model without BBL (the free-surface MOM model, Killworth et al. 1991), the model with KE99 BBL (Killworth and Edwards 1999), and the model with the new EBBL scheme. Comparing these three sets of results, we can see that the MOM model without explicit BBL has much weaker overflow in the layer immediately above the slope. Although the overflow of dense water produces a strong barotropic circulation, as in the case with a bottom layer, it fails to propagate far either along or down the slope, contrary to expectation and observations of the behavior of true slope currents. The flow in the 482-m depth level shows a similar pattern to the barotropic flow, which suggests a weaker baroclinic effect.

With the KE99 BBL, a bottom boundary layer is developed and a region of cool, dense water can be seen moving down the slope and spreading westward in the BBL. However, the plume fails to penetrate further into the deep ocean and a significant amount of the dense water is diffused along isobaths on the upper slope.

With the new EBBL, a better defined bottom boundary layer is developed with a tonguelike shape spreading across isobath, and the dense bottom water penetrates farther south of the slope into the deep ocean. The 18°C contour (thick line) passes 42.5°N, but in Killworth and Edwards's model it only reaches 43°N. The maximum velocity at the inflow is about 60 cm s^{-1}, with velocities reaching about 100 cm s^{-1}. The plume head remains a sharper front and turns upward to the right, as expected from geostrophic adjustment theory (Whelless and Klinck 1995). It should be noted that our model gives a much thinner bottom boundary layer than that from the KE99 BBL. Both models give an expected barotropic field with cyclonic circulation near the source region, which is consistent with the results of Whelless

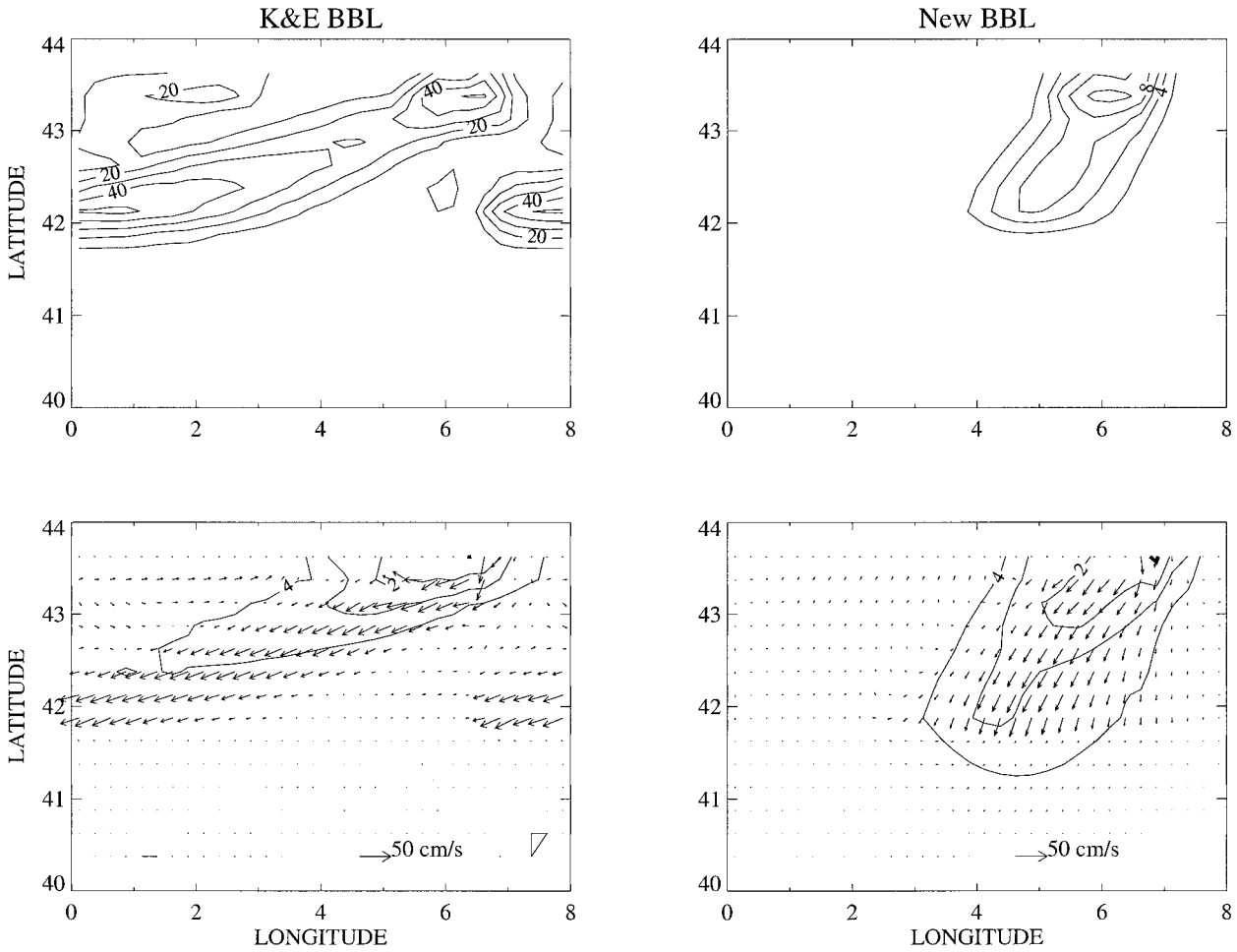

FIG. 11. Model results after 60 days of integration with decreased density contrast (0°–5°C). Shown are depth of bottom boundary layer (upper panels), bottom boundary layer temperature and velocity (lower panels), left panels from KE99 BBL, and right panels from the new EBBL.

and Klinck (1995). Comparing the horizontal level at 482-m depth, we see the new model also has an improved density field and a stronger cyclonic eddy.

As there is no analytical solution for this test problem, we choose to run a topography-following coordinate model, the *S*-Coordinate Rutgers University Model (SCRUM, Song and Haidvogel 1994) to verify our model results. Note that a similar method is also used by Beckmann and Döscher (1997) for verification of their results. For the SCRUM run, we use 20 vertical levels with a stretching parameter $\theta = 3$ and $b = 1$, allowing a higher resolution near the bottom. For a better bottom boundary layer, we use the Mellor–Yamada Level-II turbulence closure scheme to calculate the bottom boundary layer as shown by Weatherly and Martin (1978). The depth of the BBL is the height at which the turbulent kinetic energy, or equivalently, the turbulent mixing, goes to zero. Results corresponding to Figs. 4 and 5 are shown in Fig. 6. Both EBBL and SCRUM generate a similar bottom boundary layer spreading across isobaths in a tonguelike distribution. Bottom flows are initially directed offshore, with subsequent anticyclonic recirculation and upslope transports. However, SCRUM gives a much weaker cyclonic circulation near the source region in both its barotropic field and the horizontal level at 482-m depth, which might be due to numerical differences in solving the barotropic mode. For example, the surface variation in the *z*-coordinate model affects the top level only, rather than being distributed into the full column of water as in the SCRUM model. More detailed results can be viewed in the cross-slope section of temperature anomaly for these three models in Fig. 7, which show that the dense water in our EBBL model can penetrate as deep as that in SCRUM, but with a rather simpler method.

4. Sensitivity analysis and momentum budget

In the previous section, we have tested and validated the model by comparing with the most recent results of

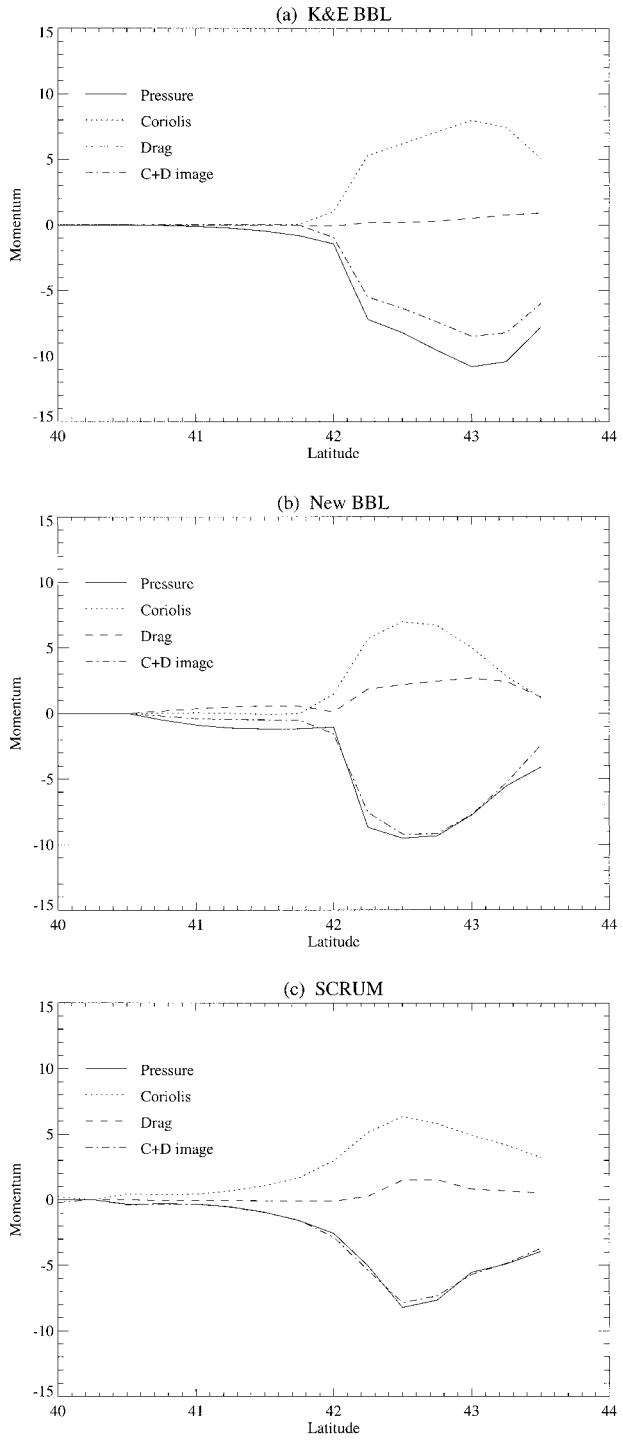

FIG. 12. Bottom layer term balance in the northward momentum equation at midlongitude in the diagram, (a) for the KE99 BBL, (b) for the new EBBL, and (c) for SCRUM. Units are cm $s^{-2} \times 10^{-3}$.

Killworth and Edwards (1999) and with the results from a topography-following coordinate model (SCRUM). This section is intended to quantify the sensitivity of the model to changes of model resolution, density contrast, and diffusion parameters and to investigate what role is played by the new pressure gradient formulation. Since the travel speed of the plume depends on the initial density contrast, we will make a short run (10 days) for the strong density contrast and a long run (60 days) for the weak density contrast in order to keep the plume within the computational domain.

a. Model resolution

In this experiment, the model resolution is increased by a factor of 2 in each spatial direction and time; all other model parameters remain unchanged. Ideally, the change of model resolution should not change the results of the overflow. The results are shown in Fig. 8 for both KE99 BBL and the new EBBL. Comparing with the results in Fig. 5, we see that our EBBL model produces a tonguelike downslope plume and a prograded dense bottom water in a similar fashion to the coarser-resolution case. It suggests that our method is less sensitive to model resolution. However, results with the KE99 BBL do not show significant improvement. Clearly, in the coarser-resolution case ($\frac{1}{4}^\circ$ and 15 levels, Fig. 5) the new EBBL produces more realistic deep water than the existing BBL with higher resolution ($\frac{1}{8}^\circ$ and 30 levels, Fig. 8), even though the latter is eight times more computationally expensive than the former one.

b. Diffusion parameters

In this experiment, we use the same parameters as in the basic experiment (Figs. 4 and 5), except for the horizontal viscosity and diffusivity coefficients, which are reduced by half. Therefore, horizontal viscosity and diffusivity coefficients are 5×10^3 and 1×10^3 m^2 s^{-1}. The results are shown in Fig. 9 for both KE99 BBL and our new EBBL. With lower viscosity and diffusivity, the KE99 BBL produces significantly different results with an unstable bottom layer and shallower penetration of dense water. In contrast, the EBBL produces a similar solution to that in the basic run (see Fig. 5) except for a sharper plume head as expected in the low diffusion case. This consistency indicates that our EBBL is not very sensitive to the horizontal viscosity and diffusivity coefficients.

c. Density contrast

In this experiment, we first increase the density contrast by a factor of 2, that is, the cold water is 0°C and the warm water is still 20°C. This strong density contrast is clearly unrealistic, but it is purposely designed to test the model's ability to handle extreme cases. The results are shown in Fig. 10 with the KE99 BBL and with the new EBBL. Although both models produce a bottom plume as expected, there are significant differences. The boundary layer depth in the KE99 BBL is thicker with maximum thickness of 200 m, spreads all over the slope

region, and the densest water travels farther along isobaths with a diffusing plume head. On the other hand, the boundary layer depth in the EBBL model has a maximum depth of 120 m, is constrained to a more limited area, and the dense bottom water moves southwestward with a sharp plume head. Density concentrations are strongly bottom intensified, as expected for a thin dense water plume.

In the second experiment, we decrease the density contrast by setting the cold water to 0°C and warm water 5°C, which is closer to the density contrast of the Denmark Strait overflow problem (Jungclaus and Backhaus 1994). The results are given in Fig. 11 for both methods. Again we see big differences between these two methods and the shape of the plume is changed dramatically. These two experiments demonstrate that the proposed EBBL is robust and works well for both extreme cases.

d. Momentum budget

To get more insight into the dynamical processes of the simulated plume, we carry out the following momentum budget analysis. The principal dynamical balance for the baroclinic velocities is among the pressure, Coriolis, and the bottom drag. The other terms in the equation are relatively small (Whelless and Klinck 1995) and are therefore not analyzed here. The importance of the bottom pressure gradient force is best revealed by examining the momentum balance in the bottom layer at a given longitude section. Figure 12 shows the three major terms in the v_B equation (2.9) along a north–south section in the middle of the domain for KE99 BBL, our new EBBL, and SCRUM. The balance of the pressure gradient term with the Coriolis and bottom drag terms in the new model is significantly improved compared with the KE99 BBL results, although it is not as good as that in SCRUM. As we know that the development of the plume has reached a quasi-steady state after 30 days simulation by comparing the results at day 30 in Fig. 4 with that at day 60 of KE99 BBL (their Fig. 4), the momentum tendency is negligible and the unbalanced part is compensated mainly from diffusion. This tells us the KE99 model, although greatly improved over the original MOM model, is still too diffusive, which is consistent with their results shown in Fig. 4 that the plume is mostly diffused along isobaths.

5. Summary and conclusions

The importance of adequate topographic representation in *z*-coordinate ocean models has been realized recently by large-scale ocean modelers. Winton et al. (1998), through process experiments, conclude that the model solutions will converge when the *z*-coordinate model has sufficient vertical resolution to resolve the bottom viscous layer and horizontal grid spacing equal to its vertical grid spacing divided by the maximum slope (i.e., $\Delta x \approx \Delta z/\alpha$, where α is the slope). Since a typical vertical scale for the overflow plumes is 100 m and a typical slope is 0.01, these conditions imply that resolution on the order of 30–50 m in the vertical and 3–5 km in the horizontal will be needed to represent frictional sinking with reasonable accuracy. This resolution is prohibitive on today's computer. This is especially true for climate simulations that require thousands of modeled years to establish a balance between downward advection of cold water and diffusion of heat.

To tackle this problem, we have developed an EBBL scheme for improving the topographic representation of *z*-coordinate ocean models. The scheme is based on three combined techniques of an embedded topography-following slab (Beckmann and Döscher 1997), an explicit turbulent bottom boundary layer (BBL) (Killworth and Edwards 1999), and a generalized pressure gradient formulation (Song 1998) for coupling the interior *z*-level model and the bottom layer model. The model is tested extensively with the known dynamics of dense slope flows and three conclusions are reached.

- Our method is simple, cost effective, and works very well for the test problem.
- The EBBL scheme is not very sensitive to model resolution and parameters.
- The downslope pressure force plays an important role in simulating dense slope flows.

In the introduction, we pointed out three consequences of using a steplike approximation of bottom topography. Although we only focused on the dense slope flow in this test problem, the other two issues could in theory be improved with the topography-following feature in the EBBL scheme, but further work, such as testing the form stress problem proposed by Haidvogel and Bechmann (1998), is needed. Clearly, further applications of the proposed EBBL to more realistic model configurations are needed. It is our intention to apply the EBBL to a realistic ocean model (Chao et al. 1996) in the near future. Lastly, it should be pointed out that our EBBL scheme is not limited to *z*-coordinate models.

Acknowledgments. The research described in this manuscript was carried out at the Jet Propulsion Laboratory (JPL), California Institute of Technology, under a contract with the National Aeronautics and Space Administration (NASA). Support from NASA High Performance Computing and Communication (HPCC) is also acknowledged. Computations were performed on the Cray J-90 through the JPL Supercomputing project. Thanks to P. D. Killworth and N. R. Edwards for providing their BBL code and valuable discussions, and to L.-L. Fu at JPL for his continuous support. Comments from two anonymous reviewers helped to improve the original manuscript.

REFERENCES

Adcroft, A., C. Hill, and J. Marshall, 1997: Representation of topography by shaved cells in a height coordinate ocean model. *Mon. Wea. Rev.,* **125,** 2293–2315.

Arakawa, A., and M. J. Suarez, 1983: Vertical differencing of the primitive equations in sigma coordinates. *Mon. Wea. Rev.*, **111,** 34–45.

Beckmann, A., and R. Döscher, 1997: A method for improved representation of dense water spreading over topography in geopotential-coordinate models. *J. Phys. Oceanogr.,* **27,** 581–591.

Broecker, W. S., 1991: The great ocean conveyor. *Oceanography,* **4,** 79–89.

Bryan, K., 1969: A numerical method for the study of the circulation of the world ocean, *J. Comput. Phys.*, **4** (3), 347–376.

Bryden, H. L., and T. H. Kinder, 1991: Steady two-layer exchange through the Strait of Gibraltar. *Deep-Sea Res.*, **93,** 1281–1292.

Chao, Y., A. Gangopadhyay, F. O. Bryan, and W. R. Holland, 1996: Modeling the Gulf Stream system: How far from reality? *Geophys. Res. Lett.,* **23** (22), 3155–3158.

Cox, M. D., 1984: A primitive equation, 3-dimensional model of the ocean. GFDL Ocean Group Tech. Rep. No. 1, 143 pp. [Available from Geophysical Fluid Dynamics Laboratory/NOAA, P.O. Box 308, Princeton, NJ 08542-0308.]

Dickson, R. R., and J. Brown, 1994: The production of North Atlantic Deep Water: Sources, rates and pathways. *J. Geophys. Res.*, **99,** 12 319–12 341.

Gerdes, R., 1993: A primitive equation ocean circulation model using a general vertical coordinate transformation, I. Description and testing of the model. *J. Geophys. Res.*, **98** (C8), 14 683–14 701.

Haidvogel, D. B., and F. O. Bryan, 1992: Ocean general circulation modeling. *Climate System Modeling,* K. E. Trenberth, Ed., Cambridge University Press, 371–412.

——, and A. Beckmann, 1998: Numerical models of the coastal ocean. *The Sea,* K. H. Brink and A. R. Robinson, Eds., Vol. 10, John Wiley and Sons, 457–482.

Haney, R. L., 1991: On the pressure gradient force over steep topography in sigma coordinate ocean models. *J. Phys. Oceanogr.*, **21,** 610–619.

Hughes, C. W., 1995: A warning about topography in the Cox code, *Ocean Modelling* (unpublished manuscript), **106,** 8–11.

Jungclaus, J. H., and J. O. Backhaus, 1994: Application of a transient reduced gravity plume model to the Denmark Strait overflow. *J. Geophys. Res.*, **99,** 12 375–12 396.

Killworth, P. D., and N. R. Edwards, 1999: A turbulent bottom boundary layer code for use in numerical ocean models. *J. Phys. Oceanogr.,* **29,** 1221–1238.

——, D. Stainforth, D. J. Webb, and S. M. Paterson, 1991: The development of a free-surface Bryan–Cox–Semtner model. *J. Phys. Oceanogr.,* **21,** 1333–1348.

Marshall, J., C. Hill, L. Perelman, and A. Adcroft, 1997: Hydrostatic, quasi-hydrostatic and non-hydrostatic ocean modeling. *J. Geophys. Res.,* **102** (C3), 5733–5752.

McWilliams, J. C., 1996: Modeling the oceanic general circulation. *Annu. Rev. Fluid Mech.,* **28,** 215–248.

Middleton, J. F., and D. Ramsden, 1996: The revolution of the bottom boundary layer on the sloping continental shelf: A numerical study. *J. Geophys. Res.*, **101** (C8), 18 061–18 077.

Price, J. F., and M. O. Baringer, 1994: Outflows and deep water production by marginal seas. *Progress in Oceanography,* Vol. 33, Pergamon, 161–200.

Roberts, M. J., and R. A. Wood, 1997: Topographic sensitivity studies with a Bryan–Cox-type ocean model. *J. Phys. Oceanogr.,* **27,** 823–836.

Semtner, A. J., 1995: Modeling ocean circulation. *Science,* **269,** 1379–1385.

Song, Y. T., 1998: A general pressure gradient formulation for ocean models. Part I: Scheme design and diagnostic analysis. *Mon. Wea. Rev.,* **126,** 3213–3230.

——, and D. Haidvogel, 1994: A semi-implicit ocean circulation model using a generalized topography-following coordinate system. *J. Comput. Phys.*, **115** (1), 228–244.

——, and D. Wright, 1998: A general pressure gradient formulation for ocean models. Part II: Energy, momentum, and bottom torque consistency. *Mon. Wea. Rev.,* **126,** 3231–3247.

Treguier, A. M., and J. C. McWilliams, 1990: Topographic influences on wind-driven, stratified flow in a β-plane channel: An idealized model for the Antarctic Circumpolar Current. *J. Phys. Oceanogr.,* **20,** 321–343.

Trowbridge, J. H., and S. J. Lentz, 1991: Asymmetric behavior of an oceanic boundary layer above a sloping bottom. *J. Phys. Oceanogr.,* **21,** 1171–1185.

Weatherly, G. L., and P. J. Martin, 1978: On the structure and dynamics of the oceanic bottom boundary layer. *J. Phys. Oceanogr.,* **8,** 557–570.

Whelless, G. H., and J. M. Klinck, 1995: The evolution of density-driven circulation over sloping bottom topography. *J. Phys. Oceanogr.,* **25,** 888–901.

Whitehead, J. A., 1989: Giant Ocean Cataracts. *Sci. Amer.*, February, 50–57.

Winton, M., R. Hallberg, and A. Gnanadesikan, 1998: Simulation of density-driven frictional downslope flow in *z*-coordinate ocean models. *J. Phys. Oceanogr.,* **28,** 2163–2174.

Zilitinkevich, S., and D. V. Mironov, 1996: A multi-limit formulation for the equilibrium depth of a stably stratified boundary layer. *Bound.-Layer Meteor.,* **81,** 325–351.